Nondestructive Electromagnetic Characterization of Uniaxial Sheet Media Using a Two-Flanged Rectangular Waveguide Probe

Neil Rogers, Michael Havrilla, *Senior Member, IEEE*, Milo W. Hyde, IV, *Senior Member, IEEE*, and Alexander Knisely

***Abstract*— A nondestructive evaluation technique for determining complex permittivities and permeabilities of uniaxial anisotropic sheet media is presented. An existing technique, the two-flanged waveguide measurement technique (tFWMT), has demonstrated good results for the nondestructive electromagnetic characterization of isotropic materials. This article extends the tFWMT for uniaxially anisotropic materials and presents the experimental determination of the permittivity and permeability of uniaxially anisotropic media. The measured scattering parameters are compared to theoretical scattering parameters, and the complex permittivity and permeability are extracted using a nonlinear least squares method. To find theoretical scattering parameters, Love's equivalence principle and the spectral-domain Green's function are used to form a set of coupled magnetic-field integral equations (MFIEs). This set of coupled MFIEs is solved utilizing the method of moments. To validate the new method, electromagnetic characterization of two honeycomb materials is made by using the two-flanged waveguides measurement technique and the results are compared to those obtained using the established methods.**

***Index Terms*— Anisotropic materials, nondestructive characterization, permittivity, uniaxial.**

I. Introduction

RECENT advancements in fabrication capabilities have renewed interest in the electromagnetic characterization of complex media, as many metamaterials are anisotropic and/or inhomogeneous. Additionally, for composite materials, anisotropy can be introduced by load, strain, misalignment, or damage through the manufacturing process [1], [2]. Methods for obtaining the constitutive parameters for isotropic materials are well understood and widely employed [3]–[8]. Therefore, it is crucial to develop a practical method for the electromagnetic characterization of anisotropic materials.

Characterization methods for anisotropic media are significantly more difficult due to the inherent complexity of the resultant form of Maxwell's equations and the requirement for a greater number of measurements. Destructive, free space, and cavity methods, such as those detailed in [9]–[16] can be very useful, but they require a precisely cut sample, which is not always available for many practical scenarios. Recently, the two-flanged waveguide measurement technique (tFWMT) employed in [5], [8], and [17] has been demonstrated effectively in extracting both permittivity (ε_r) and permeability (μ_r) of isotropic materials. Additionally, the coaxial clamped probe (CCP) method was employed [18] in extracting the constitutive parameters of anisotropic materials. However, due to well-known issues with characterizing low-permittivity materials, the uncertainty associated with the CCP method is greater than that of the tFMWT.

This article advances the state of the art with regard to nondestructive electromagnetic characterization by extending the theory of the tFMWT to account for uniaxial anisotropy and furthermore presents the significant result of demonstrating the method experimentally. It is shown that the present method reduces much of the uncertainty associated with the CCP, but maintaining similar accuracy. Additionally, this article provides a promising foundation for the electromagnetic characterization of more general classes of complex media, such as gyrotropic.

The theoretical development of the tFWMT for uniaxial media is presented in Section II. Following the previous work, this analysis focuses on the derivation of the theoretical scattering parameters for uniaxial media, which are ultimately required for permittivity and permeability extraction. These parameters are formulated by first applying Love's equivalence principle and then enforcing the continuity of tangential fields. The resulting coupled system of magnetic-field integral equations (MFIEs) is subsequently solved for the theoretical scattering parameters using the method of moments (MoM). Finally, the desired complex permittivity and permeability tensor elements are determined via a nonlinear least squares minimization of the difference between the theoretical and measured scattering parameters.

To validate the new tFWMT, the experimental results of two non-magnetic honeycomb materials are presented in Section III. The permittivity tensor results obtained using the extended tFWMT are compared with those obtained using a traditional destructive characterization method. The tFMWT's sensitivities to common experimental errors are also investigated.

Manuscript received October 1, 2018; revised April 4, 2019; accepted June 6, 2019. Date of publication July 2, 2019; date of current version May 12, 2020. The Associate Editor coordinating the review process was Kamel Haddadi. *(Corresponding author: Neil Rogers.)*

The authors are with the Department of Electrical and Computer Engineering, Air Force Institute of Technology, Wright-Patterson Air Force Base, Dayton, OH 45433 USA, and also with the Department of Electrical and Computer Engineering, United States Air Force Academy, Colorado Springs, CO 80840 USA (e-mail: neil.rogers@us.af.mil).

Color versions of one or more of the figures in this article are available online at http://ieeexplore.ieee.org.

Digital Object Identifier 10.1109/TIM.2019.2925408

II. Two-Flanged Waveguide Measurement Technique

In general, the complex permittivity and permeability tensor elements, $\overleftrightarrow{\varepsilon} = \hat{x}\hat{x}\varepsilon_t + \hat{y}\hat{y}\varepsilon_t + \hat{z}\hat{z}\varepsilon_z$ and $\overleftrightarrow{\mu} = \hat{x}\hat{x}\mu_t + \hat{y}\hat{y}\mu_t + \hat{z}\hat{z}\mu_z$, can be determined via a nonlinear least squares minimization of the difference between the theoretical and experimental scattering parameters

$$\underset{\varepsilon_t,\varepsilon_z,\mu_t,\mu_z\in\mathbb{C}}{\arg\min}\left\|\begin{bmatrix} S_{11}^{\text{thy}}(f,d;\varepsilon_t,\varepsilon_z,\mu_t,\mu_z)-S_{11}^{\text{exp}}(f)\\ S_{21}^{\text{thy}}(f,d;\varepsilon_t,\varepsilon_z,\mu_t,\mu_z)-S_{21}^{\text{exp}}(f)\\ S_{12}^{\text{thy}}(f,d;\varepsilon_t,\varepsilon_z,\mu_t,\mu_z)-S_{12}^{\text{exp}}(f)\\ S_{22}^{\text{thy}}(f,d;\varepsilon_t,\varepsilon_z,\mu_t,\mu_z)-S_{22}^{\text{exp}}(f)\end{bmatrix}\right\|_2 \quad (1)$$

where f is the frequency and d is the thickness of the material under test (MUT). Note, in the case of Fig. 1, S_{11} is not independent of S_{22} nor is S_{21} independent of S_{12}, and therefore, only enough independent measurements are available to extract two of the four uniaxial constitutive parameters. The dependent measurements are included to minimize experimental errors. In order to extract all four parameters, an additional set of independent measurements is necessary. For some materials, a two-thickness method (TTM) [3] could be used (when a suitable second thickness of the MUT is available) or the two-layer method (TLM) [19].

In developing the theoretical coefficients, Love's equivalence principle, continuity of tangential fields, and the MoM are utilized to arrive at a set of coupled MFIEs. The MFIEs contain six integrals, which if calculated numerically, would require tremendous computational resources, given the number of function evaluations required by the nonlinear least squares solver. Therefore, the integrals are evaluated in the spectral domain using complex plane analysis, resulting in a single remaining integral that is evaluated numerically.

A. MFIE Development and MoM Solution

The physical configuration of the tFWMT geometry is shown in Fig. 1. The first step in developing the MFIEs is to determine the fields in each region (I–III). Since boundary conditions are enforced at $z = 0$ and $z = d$, only the tangential fields, indicated by the subscript t, are reported here. The tangential fields in Regions I and III are

$$\vec{E}_{t,I} = a_1^+\vec{e}_1 e^{-\gamma_1 z} + \sum_{q=1}^{Q} a_q^-\vec{e}_q e^{\gamma_q z}$$
$$\vec{H}_{t,I} = a_1^+\vec{h}_1 e^{-\gamma_1 z} - \sum_{q=1}^{Q} a_q^-\vec{h}_q e^{\gamma_q z} \quad (2)$$

and

$$\vec{E}_{t,III} = \sum_{q=1}^{Q} b_q^+\vec{e}_q e^{-\gamma_q(z-d)}$$
$$\vec{H}_{t,III} = \sum_{q=1}^{Q} b_q^+\vec{h}_q e^{-\gamma_q(z-d)} \quad (3)$$

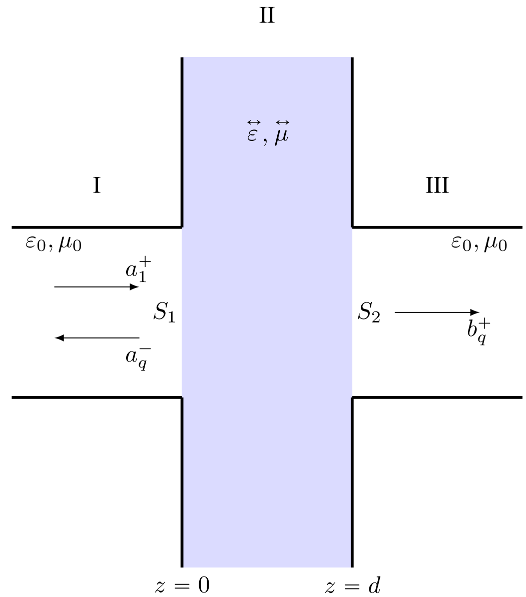

Fig. 1. Geometry of the tFWMT. The MUT of thickness d and parameters $\overleftrightarrow{\varepsilon}$ and $\overleftrightarrow{\mu}$ is clamped between two free-space-filled infinitely flanged $a \times b$ RWGs. The complex amplitudes of the incident mode, the reflected modes, and the transmitted modes are specified by a_1^+, a_q^-, and b_q^+, respectively.

where q represents the mode index (m and n combination), $\vec{e}_q$ and $\vec{h}_q$ are the tangential components of the rectangular waveguide (RWG) electric and magnetic field distributions (both TE^z and TM^z), respectively [20], and $\gamma_q = ((m\pi/a)^2 + (n\pi/b)^2 - k_0^2)^{1/2}$. Here, $k_0 = \omega\sqrt{\varepsilon_0\mu_0}$ is the free-space wavenumber and $\omega = 2\pi f$. Note that the tFWMT symmetry condition discussed in [5] holds here. Therefore, $q = 1$ describes the TE$_{10}^z$ mode, $q = 2$ describes the TE$_{30}^z$ mode, and so on. A list of the first 20 values of q and the corresponding modes is given in [21].

In anticipation of enforcing the continuity of tangential fields and a subsequent MoM solution, the electric field given in (2) is evaluated at $z = 0$ (denoted by $\vec{e}_{a1}$) and tested using the qth mode of the electric field. Rearranging (2) and utilizing mode orthogonality, one obtains

$$a_q^- = \int_{S_1} \vec{e}_q \cdot \vec{e}_{a1} dS - a_1^+\delta_{q1} \quad (4)$$

with

$$\delta_{q1} = \begin{cases} 1 & \ldots q = 1 \\ 0 & \ldots q \neq 1. \end{cases} \quad (5)$$

Performing similar operations on the electric field of (3) evaluated at $z = d$ (denoted by $\vec{e}_{a2}$), one finds

$$b_q^+ = \int_{S_2} \vec{e}_q \cdot \vec{e}_{a2} dS. \quad (6)$$

Substitution of (4) and (6) into the magnetic fields of Regions I and III evaluated at $z = 0$ and $z = d$, respectively, yields

$$\vec{H}_{t,I}(z=0) = 2a_1^+\vec{h}_1 - \sum_{q=1}^{Q}\left(\int_{S_1}\vec{e}_q \cdot \vec{e}_{a1} dS\right)\vec{h}_q \quad (7)$$

$$\vec{H}_{t,III}(z=d) = \sum_{q=1}^{Q} \left(\int_{S_2} \vec{e}_q \cdot \vec{e}_{a2} dS \right) \vec{h}_q. \quad (8)$$

Next, an expression is obtained for the tangential magnetic field in the parallel-plate region of the tFWMT (Region II). This expression is given in the familiar Green's function form via Love's equivalence principle

$$\vec{H}_t^{\mathrm{pp}}(\vec{\rho}, z) = \sum_{c=1}^{2} \int_{S_c'} \overleftrightarrow{G}_{hh}(\vec{\rho}, z|\vec{\rho}_c{}', z_c') \cdot \vec{J}_{hc}(\vec{\rho}_c{}', z_c') dS_c'. \quad (9)$$

Defining $\vec{\lambda}_\rho = \hat{x}\lambda_x + \hat{y}\lambda_y$ and $d^2\lambda_\rho = d\lambda_x d\lambda_y$, the dyadic spatial-domain Green's function of (9) is the inverse transform of the spectral-domain Green's function, which is given explicitly in [22]

$$\begin{aligned} &\overleftrightarrow{G}_{hh}(\vec{\rho}, z|\vec{\rho}\,', z\,') \\ &\quad = \frac{1}{4\pi^2} \iint_{-\infty}^{\infty} \overleftrightarrow{\tilde{G}}_{hh}\,(\vec{\lambda}_\rho, z|z\,') e^{j\vec{\lambda}_\rho \cdot (\vec{\rho}-\vec{\rho}\,')} d^2\lambda_\rho \end{aligned} \quad (10)$$

with $\vec{J}_{h1} = -\hat{z} \times \vec{e}_{a1}$ and $\vec{J}_{h2} = \hat{z} \times \vec{e}_{a2}$.

In the summation notation used in (9), the c index refers to the aperture under consideration. Note that because the tFWMT is a two-port device, there will be a "self" term and a "cross" term to account for the two source and observation points ($z, z' = 0$ and $z, z' = d$). Here, the unprimed coordinates correspond to the observation points, while the primed coordinates refer to the location of the source. The single overset tilde represents a quantity that has been Fourier transformed on the transverse spatial variables, x and y. The first h in the hh subscript on the Green's function refers to the observed transverse magnetic field, while the second h refers to the source that maintains the field—an equivalent transverse magnetic surface current in this case.

Finally, enforcing the continuity of the tangential magnetic fields at $z = 0$ and $z = d$ leads to the desired system of coupled MFIEs

$$2a_1^+ \vec{h}_1 - \sum_{q=1}^{Q} \left(\int_{S_1} \vec{e}_q \cdot \vec{e}_{a1} dS \right) \vec{h}_q = \sum_{c=1}^{2} (-1)^c \frac{1}{4\pi^2} \Theta_{1c} \quad (11)$$

and

$$\sum_{q=1}^{Q} \left(\int_{S_2} \vec{e}_q \cdot \vec{e}_{s2} dS \right) \vec{h}_q = \sum_{c=1}^{2} (-1)^c \frac{1}{4\pi^2} \Theta_{2c} \quad (12)$$

where

$$\begin{aligned} \Theta_{1c} = \iint_{-\infty}^{\infty} \Bigg\{ \int_0^b \int_0^a & \overleftrightarrow{\tilde{G}}_{hh}\,(\vec{\lambda}_\rho, z_1^+|z_c') \cdot \left[\hat{z} \times \vec{e}_{ac}(\vec{r}\,'_c) \right] \\ & e^{j\vec{\lambda}_\rho \cdot (\vec{\rho}-\vec{\rho}\,')} dx'dy' \Bigg\} d^2\lambda_\rho \end{aligned} \quad (13)$$

and

$$\begin{aligned} \Theta_{2c} = \iint_{-\infty}^{\infty} \Bigg\{ \int_0^b \int_0^a & \overleftrightarrow{\tilde{G}}_{hh}\,(\vec{\lambda}_\rho, z_2^-|z_c') \cdot \left[\hat{z} \times \vec{e}_{ac}(\vec{r}\,'_c) \right] \\ & e^{j\vec{\lambda}_\rho \cdot (\vec{\rho}-\vec{\rho}\,')} dx'dy' \Bigg\} d^2\lambda_\rho. \end{aligned} \quad (14)$$

In Θ_{1c} and Θ_{2c}, z_1^+ is the position just to the right of $z = 0$ and z_2^- is the position just to the left of $z = d$. The subscript index c denotes the appropriate aperture for the source terms. Furthermore, throughout this article, primed variables correlate with source terms and unprimed variables correlate with observation terms. The MoM is used to solve the above-mentioned system of MFIEs. The unknown aperture electric fields are expanded using the tangential RWG electric field distributions given in (2) and (3), namely

$$\begin{aligned} \vec{e}_{a1} &= \sum_{w=1}^{W} a_1^+ \, C_w^{(1)} \vec{e}_w \\ \vec{e}_{a2} &= \sum_{w=1}^{W} a_1^+ \, C_w^{(2)} \vec{e}_w. \end{aligned} \quad (15)$$

Note that the generic mode index q has been replaced with a mode index w, which refers specifically to the basis functions to represent the TE^z/TM^z modes. As was previously mentioned, $w = 1$ refers to the TE$_{10}$ mode, $w = 2$ refers to the TE$_{30}$ mode, and so on. Furthermore, in some cases, it is necessary to distinguish between whether the x and y variations in the modes, which are typically denoted by m and n, are specifically associated with the testing or basis functions. In these cases, the testing functions are designated by the notation TE/TM$^z_{m_v n_v}$ and the basis functions by the notation TE/TM$^z_{m_w n_w}$. The resulting equations are then tested using the tangential RWG magnetic field distributions also provided in (2) and (3). In this case, v is used as the mode index for the testing modes, namely

$$\begin{aligned} &\int_{S_1} \vec{h}_v(\vec{\rho}_1) \cdot \{(11)\} dS_1 \\ &\int_{S_2} \vec{h}_v(\vec{\rho}_2) \cdot \{(12)\} dS_2 \end{aligned} \quad (16)$$

where the expansion indices represent the total number of modes considered, thus determining the accuracy of the theoretical solution. After applying the testing and expansion functions, a $2Q \times 2Q$ system of equations is formed, namely

$$\underbrace{\begin{bmatrix} A^{(11)} & A^{(12)} \\ A^{(21)} & A^{(22)} \end{bmatrix}}_{2Q\times 2Q} \underbrace{\begin{bmatrix} C^{(1)} \\ C^{(2)} \end{bmatrix}}_{2Q\times 1} = \underbrace{\begin{bmatrix} B^{(1)} \\ B^{(2)} \end{bmatrix}}_{2Q\times 1} \quad (17)$$

where

$$\begin{aligned} A_{vw}^{(11)} &= \int_{S_1} \vec{h}_v(\vec{r}_1) \cdot \vec{h}_w(\vec{r}_1) dS_1 \\ &\quad - \frac{Z_w}{4\pi^2} \iint_{-\infty}^{\infty} \left(\vec{\Lambda}_{v,1} \cdot \overleftrightarrow{\tilde{G}}_{hh}\,(\vec{\lambda}_\rho, z_1|z_1') \cdot \vec{\Lambda}_{w,1} \right) d^2\lambda_\rho \\ A_{vw}^{(12)} &= \frac{Z_w}{4\pi^2} \iint_{-\infty}^{\infty} \left(\vec{\Lambda}_{v,1} \cdot \overleftrightarrow{\tilde{G}}_{hh}\,(\vec{\lambda}_\rho, z_1|z_2') \cdot \vec{\Lambda}_{w,2} \right) d^2\lambda_\rho \\ B^{(1)} &= 2 \int_{S_1} \vec{h}_v(\vec{r}_1) \cdot \vec{h}_1(\vec{r}_1) dS_1 \\ B^{(2)} &= 0 \\ \vec{\Lambda}_{v,\alpha} &= \int_0^b \int_0^a \vec{h}_v(\vec{r}_\alpha) e^{j\vec{\lambda}_\rho \cdot \vec{\rho}} \, dxdy \\ \vec{\Lambda}_{w,\alpha} &= \int_0^b \int_0^a \vec{h}_w(\vec{r}\,'_\alpha) e^{-j\vec{\lambda}_\rho \cdot \vec{\rho}\,'} dx'dy'. \end{aligned} \quad (18)$$

Here, the double integrals depicted by the Λ notation represent the total observed (unprimed variables) and source (primed variables) magnetic fields at a given aperture (α subscript). Furthermore, the Z_w terms represent the wave (and mode) impedance for the waveguide region. Note that $\alpha = 1, 2$ and $A_{vw}^{(22)} = A_{vw}^{(11)}$ and $A_{vw}^{(21)} = A_{vw}^{(12)}$ due to the symmetry of the tFWMT and electromagnetic reciprocity, respectively.

Solving for $\vec{\mathbf{C}}$ in (17) leads to the theoretical scattering coefficients necessary to solve (1) via nonlinear least squares. The theoretical scattering coefficients are found from the MoM expansion coefficients [see (4) and (6)] by

$$S_{11}^{\text{thy}} = \frac{a_1^-}{a_1^+} = C_1^{(1)} - 1 \tag{19}$$

$$S_{21}^{\text{thy}} = \frac{b_1^+}{a_1^+} = C_1^{(2)} \tag{20}$$

where the theoretical transmission and reflection coefficients are found from the first element in each subarray of $\vec{\mathbf{C}}$, which corresponds to the dominant propagation mode in the waveguide. Note that solution convergence is typically reached using a small number, Q, of higher order modes.

B. Evaluation of the λ_y Integral via Complex Plane Analysis

Although a complete solution to the minimization problem in (1) has been determined, the solution may be expedited considerably by the analytical evaluation of some of the integrals of (18). Evaluation of the $\vec{\Lambda}_v$ and $\vec{\Lambda}_w$ spatial integrals over the observation variables x and y and the source variables x' and y', respectively, is very straightforward. Furthermore, in one of the main departures from the isotropic case, the Green's function is a dyad with off-diagonal elements, thereby requiring expansion of the dot products. Here, the MoM matrix elements $A_{vw}^{(11)}$ are evaluated. The evaluation of the others follows in a similar manner.

After evaluating the $\vec{\Lambda}_v$ and $\vec{\Lambda}_w$ spatial integrals, $A_{vw}^{(11)}$ takes the form

$$\begin{aligned} A_{vw}^{(11)} &= \delta_{v,w}\left(\frac{ab}{4}\right)\left[\left(M_{xv}^h\right)^2 + \left(M_{yv}^h\right)^2\right](1+\delta_{w_m,0}) \\ &\quad - \frac{Z_w}{4\pi^2}\int_{-\infty}^{\infty}\Bigg\{A_{\lambda_x}^{(11)}\int_{-\infty}^{\infty}\Big[M_{xv}^h M_{xw}^h k_{xv}k_{xw}\lambda_y^2 \widetilde{G}_{hh,xx}^{00} \\ &\qquad + M_{xv}^h M_{yw}^h k_{xv}k_{yw}\lambda_x\lambda_y \widetilde{G}_{hh,xy}^{00} \\ &\qquad + M_{yv}^h M_{xw}^h k_{xv}k_{yw}\lambda_x\lambda_y \widetilde{G}_{hh,yx}^{00} \\ &\qquad + M_{yv}^h M_{yw}^h k_{yv}k_{yw}\lambda_x^2 \widetilde{G}_{hh,yy}^{00}\Big] \\ &\qquad \times A_{\lambda_y}^{(11)} d\lambda_y\Bigg\} d\lambda_x \end{aligned} \tag{21}$$

with

$$A_{\lambda_x}^{(11)} = \frac{\left(1-(-1)^{m_v}e^{j\lambda_x a}\right)\left(1-(-1)^{m_w}e^{-j\lambda_x a}\right)}{(\lambda_x+k_{xv})(\lambda_x-k_{xv})(\lambda_x+k_{xw})(\lambda_x-k_{xw})} \tag{22}$$

$$A_{\lambda_y}^{(11)} = \frac{\left(1-(-1)^{n_v}e^{j\lambda_y b}\right)\left(1-(-1)^{n_w}e^{-j\lambda_y b}\right)}{\left(\lambda_y+k_{yv}\right)\left(\lambda_y-k_{yv}\right)\left(\lambda_y+k_{yw}\right)\left(\lambda_y-k_{yw}\right)} \tag{23}$$

where the notation for the Green's functions has been condensed such that

$$\widetilde{G}_{hh,xx}^{00} = \widetilde{G}_{hh,xx}(z=0|z'=0). \tag{24}$$

Here, the M and Z terms are dependent on whether the mode is TE^z or TM^z

$$\ldots\text{for TE}_{m_\alpha n_\alpha}^z \begin{cases} M_{x\alpha}^h = k_{x\alpha}/Z_\alpha \\ M_{y\alpha}^h = k_{y\alpha}/Z_\alpha \\ Z_\alpha = j\omega\mu_0/\gamma_{z\alpha} \end{cases}$$

$$\ldots\text{for TM}_{m_\alpha n_\alpha}^z \begin{cases} M_{x\alpha}^h = k_{y\alpha} \\ M_{y\alpha}^h = -k_{x\alpha} \\ Z_\alpha = \gamma_{z\alpha}/(j\omega\varepsilon_0) \end{cases}$$

where $k_{x\alpha} = m_\alpha\pi/a$, $k_{y\alpha} = n_\alpha\pi/b$, and $\alpha = v, w$ (specifying the testing or basis functions, respectively). Additionally, since propagation in only the z-direction is assumed, γ_q has been written as $\gamma_{z\alpha}$, where, again, α specifies either the testing or basis mode.

In order to analytically evaluate the spectral-domain integrals, Cauchy's integral theorem (CIT), Jordan's lemma, and Cauchy's integral formula (CIF) are utilized. It is shown that only one of the spectral integrals can be handled analytically, as a branch cut appears in the second integral that requires much more complicated analysis. Here, the λ_y integral is evaluated analytically; the λ_x integral is evaluated numerically.

Upon inspection of the $A_{vw}^{(11)}$ term, one notes that the poles located at $\pm k_{y\alpha}$ dictate how the λ_y integral must be evaluated—the other poles not being dependent on n_α. As such, five possible cases manifest for (21) depending on the values of n_v and n_w

I $n_v = n_w = 0$
II $n_v \neq 0, n_w = 0$
III $n_v = 0, n_w \neq 0$
IV $n_v = n_w \neq 0$
V $n_v \neq n_w \neq 0$.

Each of these cases must be considered independently. This article gives a short overview of the process for I, which contains the dominant-mode-only assumption.

For I, $n_v = n_w = 0$, which leads to $k_{yv} = k_{yw} = 0$. Therefore, the λ_y integral of (21) simplifies to

$$\int_{-\infty}^{\infty}\left\{\frac{M_{xv}^h M_{xw}^h k_{xv}k_{xw}}{\lambda_y^2}\left(\frac{j\lambda_{z\theta}\lambda_x^2}{\lambda_\rho^2\omega\mu_t}\right)\left[\frac{\cos(\lambda_{z\theta}d)}{\sin(\lambda_{z\theta}d)}\right] \times\left[\left(1-e^{j\lambda_y b}\right)+\left(1-e^{-j\lambda_y b}\right)\right]\right\}d\lambda_y \tag{25}$$

where $\lambda_{z\theta} = (k_t^2 - \mu_t/\mu_z(\lambda_x^2+\lambda_y^2))^{1/2}$ and $k_t = \omega\sqrt{\varepsilon_t\mu_t}$. Examining the exponentials, one concludes that upper half-plane (UHP) closure is required for the $\exp(j\lambda_y b)$ term, while lower half-plane (LHP) closure is required for the other. Both cases are considered separately and combined for the final result. Additionally, the spectral-domain Green's function consists of a TE^z contribution and a TM^z contribution; these are also considered separately. For the sake of brevity, only the TE^z case in the UHP is considered here.

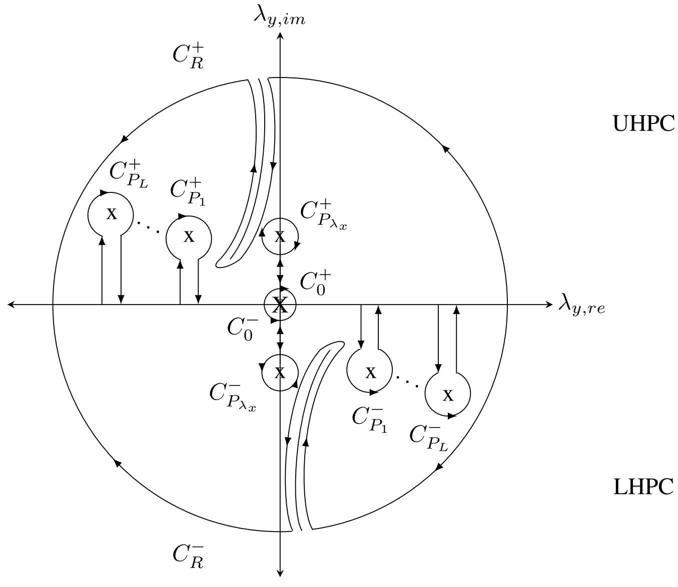

Fig. 2. Integrand of (25) in the complex λ_y plane. The branch cut arises from the square root term in $\lambda_{z\theta}$ and is removable due to the fact that the integrand is even in $\lambda_{z\theta}$. Note that the distance between the paths around the singularities is exaggerated to give a better view of the overall contour path for implementing CIT. In reality, they lie on top of each other.

The complex plane contour used in evaluating (25) is drawn in Fig. 2. In the UHP, the semicircular contour C_R^+ is shown and its contribution to the overall integral is considered in the limit as $R \to \infty$. Note that the other poles arise from the spectral-domain Green's function, i.e., the poles at $\pm j\lambda_x$ and $\pm(\mu_z/\mu_t[k_t^2 - (l\pi/d)^2] - \lambda_x^2)^{1/2}$. The CIT provides a means for calculating the value of (25) over a simply closed contour in the complex plane

$$0 = \int_{-\infty}^{\infty} + \int_{C_0^+} + \oint_{C_{j\lambda_x}^+} + \oint_{\sum C_l^+} + \overbrace{\int_{C_\infty^+}}^{0} \tag{26}$$

$$\int_{-\infty}^{\infty} = \oint_{C_0^+} + \oint_{C_{j\lambda_x}^+} + \oint_{\sum C_l^+} \tag{27}$$

$$= j\pi\,\mathrm{Res}(\lambda_y = 0) + j2\pi\,\mathrm{Res}(\lambda_y = j\lambda_x) + j2\pi \sum_l \mathrm{Res}\left(\lambda_{z\theta} = \pm\frac{\pi l}{d}\right) \tag{28}$$

where the contribution from $C_\infty^+ \to 0$ as $R \to \infty$, as stipulated by Jordan's lemma. The CIF is then employed to calculate the residue of each pole. Repeating this process for the TE^z LHP contribution and the TM^z UHP and LHP contributions and combining the results yield

$$A_{vw}^{(11)} = \frac{\delta_{vw}}{Z_v Z_w} - \frac{Z_w}{4}\left\{\int_{-\infty}^{\infty} C_{\lambda_x}\left[A_{\lambda_y}^{(11)} + B_{\lambda_y}^{(11)} + C_{\lambda_y}^{(11)} + D_{\lambda_y}^{(11)}\right] d\lambda_x\right\} \tag{29}$$

where

$$C_{\lambda_x} = \left[\frac{\left(1-(-1)^{m_v} e^{j\lambda_x a}\right)\left(1-(-1)^{m_w} e^{-j\lambda_x a}\right)}{(\lambda_x + k_{xv})(\lambda_x - k_{xv})(\lambda_x + k_{xw})(\lambda_x - k_{xw})}\right]. \tag{30}$$

In (30)

$$\begin{aligned} A_{\lambda_y}^{(11)} &= \left(\frac{M_{hx}^v M_{hx}^w m_v m_w}{a^2}\right) \\ &\quad \times \left\{ \frac{j2\pi b \lambda_{z\theta}^*}{\omega\mu_t}\left[\frac{\cos\left(\lambda_{z\theta}^* d\right)}{\sin\left(\lambda_{z\theta}^* d\right)}\right] \right. \\ &\quad - \frac{4\pi\,\mu_z \lambda_x^2}{\omega\mu_t^2\, d}\sum_{l=0}^{\infty}\left(\frac{\pi l}{d}\right)^2 \frac{\left(1 - e^{-j\lambda_{yl\theta} b}\right)}{\lambda_{yl\theta}^3\left(\lambda_{yl\theta}^2 + \lambda_x^2\right)} \\ &\quad \left. - \frac{4\pi\omega\varepsilon_z}{d}\sum_{l=0}^{\infty}\frac{\left(1 - e^{-j\lambda_{y_{l\psi}} b}\right)}{\lambda_{y_{l\psi}}\left(\lambda_{y_{l\psi}}^2 + \lambda_x^2\right)[1 + \delta_{0,l}]} \right\} \\ B_{\lambda_y}^{(11)} &= C_{\lambda_y}^{(11)} = D_{\lambda_y}^{(11)} = 0 \end{aligned} \tag{31}$$

where

$$\lambda_{yl\theta} = \sqrt{\mu_z/\mu_t\left[k_t^2 - (l\pi/d)^2\right] - \lambda_x^2} \tag{32}$$

$$\lambda_{y_{l\psi}} = \sqrt{\varepsilon_z/\varepsilon_t\left[k_t^2 - (l\pi/d)^2\right] - \lambda_x^2} \tag{33}$$

$$\lambda_{z\theta}^* = \sqrt{k_t^2 - \mu_t/\mu_z \lambda_x^2}. \tag{34}$$

The A^{11} term for the other four cases as well as the other MoM matrix elements (i.e., A^{12}, A^{21}, and A^{22}) are evaluated in a similar manner.

Although evaluating these integrals is onerous, the gain in terms of code efficiency is significant, especially when considering a large number of modes in the MoM solution.[1] Finally, note that a branch cut appears in the λ_x complex plane through the terms $\lambda_{z\theta}^*$, $\lambda_{yl\theta}$, and $\lambda_{y_{l\psi}}$. Since the integrand is not even in those terms, the branch cut contribution is not removable. Therefore, as mentioned previously, the λ_x integral is evaluated numerically.

III. Validation

A. Experimental Configuration

Material measurements were made using the configuration shown in Fig. 3, capturing both the transmission and reflection measurements from an Agilent Technologies E8362B PNA. The clamped waveguide configuration consisted of 15.24 cm × 15.24 cm × 0.635 cm (6 in × 6 in × 0.25 in) aluminum flanges attached using precision alignment pins and screws to two Maury Microwave precision X-band waveguides. The waveguides were mounted on a stable platform using optical table components and custom-machined waveguide clamps, providing excellent repeatability and precision during the measurement process.

The system was calibrated using the well-known thru–reflect–line (TRL) [23] technique, which is conducted using the built-in calibration routine of the PNA. Here, the thru measurement was made with the RWGs connected to the flange plates, which were then clamped together. For the reflect measurement, a highly reflective brass plate was placed between the flanges. Since the typical line standard would

[1]This is simply a factor of evaluating fewer integrals, as numerical integration is computationally expensive. In the most extreme cases, the nonlinear least squares solver will require dozens of function evaluations at each frequency to converge; therefore, calculating 1 integral numerically is significantly more efficient than calculating 4.

require precise custom fabrication, the normal $\lambda/4$ line standard was replaced with a modified measurement, in which the two RWGs were directly connected and a negative phase delay of 43.730 ps was manually entered to compensate for the thickness of the two 0.635-cm (0.25 in) flange plates. This time delay correlates to the thickness of the plates.

For the plots, error bars take into consideration uncertainties in the real and imaginary parts of each of the S-parameters and the thickness of the material. Therefore, we have the uncertainty for a given solution at a single frequency value as

$$\sigma_\alpha^2 = \sum_{i=1}^{2}\sum_{j=1}^{2}\left[\sigma_{S_{ij,\mathrm{real}}}\left(\frac{\partial\alpha}{\partial S_{ij,\mathrm{real}}}\right)\right]^2 + \sum_{i=1}^{2}\sum_{j=1}^{2}\left[\sigma_{S_{ij,\mathrm{imag}}}\left(\frac{\partial\alpha}{\partial S_{ij,\mathrm{imag}}}\right)\right]^2 + \sum_{k=1}^{2}\left[\sigma_{d_k}\left(\frac{\partial\alpha}{\partial d_k}\right)\right]^2 \ldots \alpha = \varepsilon_t, \varepsilon_z \mu_t, \mu_z. \quad (35)$$

In the absence of analytical expressions for the required partial derivatives, we compute the approximate numerical derivatives using the finite difference formula, with h a small change

$$\frac{\partial f(x)}{\partial x} = \frac{f(x+h) - f(x)}{h}. \quad (36)$$

Previous work has shown that material thickness is the largest contributor to uncertainty [17]. All error bars are plotted as $\pm 2\sigma$.

Because the constitutive parameters are still contained in a complex integral over λ_x, a nonlinear least squares method, in particular, MATLAB's *lsqcurvefit*, is utilized to extract the constitutive parameters. This algorithm is based on the trust-region reflective (TRR) method and is not overly sensitive to the initial guess based on the experience gained through previous work and MATLAB documentation. However, it should be noted that this method requires a number of iterations to converge, which can increase the computation time. In order to minimize the impact of convergence time, the code updates its initial guess based on the previous values. This leads to more rapid convergence over the frequencies under consideration. Furthermore, it is well known that nonlinear least-squares methods are sensitive to outliers. This article takes accurate and precise calibration as the most practical remedy.

In order to test the validity of the code, the method was utilized to extract permittivity and permeability (by assuming $\varepsilon_t = \varepsilon_z$ and $\mu_t = \mu_z$) on isotropic materials; the results showed excellent agreement with the well-known methods, such as Nicholson–Ross–Weir. This provided good confidence to proceed with uniaxial materials.

B. Experimental Results

1) Characterization of 3-D-Printed Honeycomb: Materials with occlusions arranged in a lattice structure (such as honeycomb) can be expected to demonstrate uniaxial characteristics. With recent advances in the 3-D printing technology and ease of access to such devices, patterned materials can be generated in CAD software and rapid prototyping of engineered materials is a fairly simple matter. In the course of this work, a Connex 500 was used for producing prototype materials. The "ink" used in the printer was a white nylon polymer and was utilized to make a honeycomb-patterned material. Due to resource limitations, the white nylon polymer was the only material available for use in the 3-D printer. Therefore, the occlusions of the prototype materials consisted of air. As a result, the measurements in the rest of this article are limited to non-magnetic uniaxial materials.

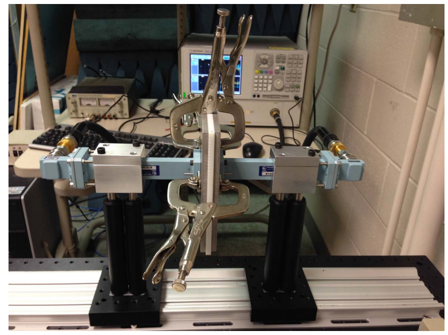

Fig. 3. tFWMT apparatus shown measuring a white nylon material. The tFWMT is supported in a mounting platform and clamps are used to ensure good contact between the MUT and the flange plates. The mounting platform and the clamps allow for excellent repeatability and precision in the measurement process.

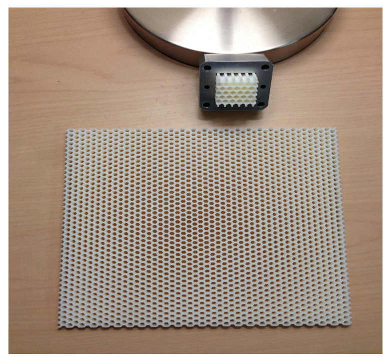

Fig. 4. Samples of the honeycomb material used for the tFWMT and WRWS measurements. The center-to-vertex spacing of each regular hexagonal cell was 1.7 mm. The center-to-center spacing of each cell was 3.5 mm.

Due to the low-loss nature of the lattice material and the air-filled hexagonal cells, the measured S-parameters were time-gated to eliminate the reflections from the edges of the plates using the method described in [17]. A photograph of the 3-D-printed honeycomb samples is shown in Fig. 4. In order to compare the values extracted via the tFWMT, the method described in [24]–[26] was used to extract the permittivity. This technique, called the waveguide-rectangular-to-waveguide-square (WRWS) technique, utilized a waveguide that slowly tapers from the standard X-band aperture to a square aperture, allowing for the measurement of a precisely cut cube sample. In this case, the sample was measured at orthogonal orientations and the values were extracted using an iterative root finding method. The WRWS ε_t and ε_z results are shown in Figs. 5 and 6, respectively.

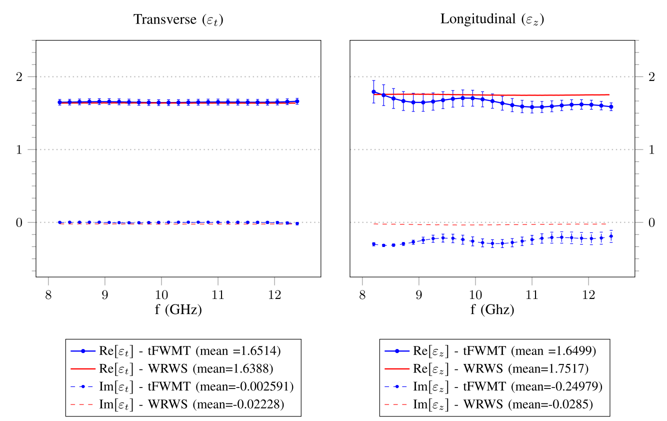

Fig. 5. Results from the tFWMT extraction performed on the honeycomb material using only the dominant mode.

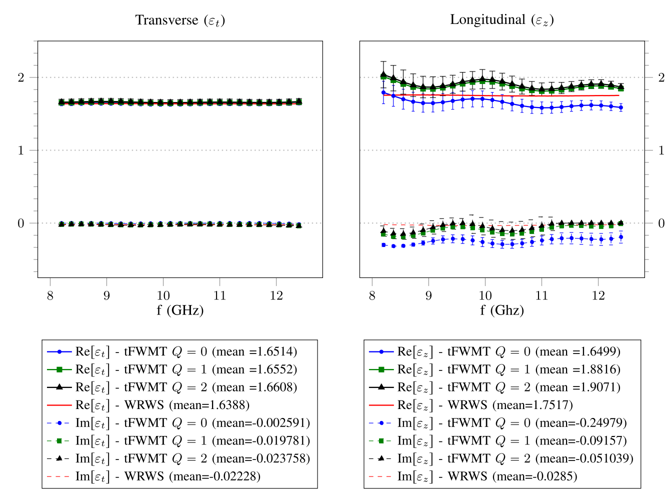

Fig. 6. Results from the tFWMT extraction performed on the honeycomb material incorporating higher order modes. Only the $\mathrm{TE}^z_{1(2q)}$ and $\mathrm{TM}^z_{1(2q)}$ modes are considered for $Q = 0,\ 1,$ and 2.

Fig. 5 shows the dominant-mode-only results using the tFWMT on the 3-D-printed honeycomb sample. It is clear from Fig. 5 that the results for the transverse permittivity ε_t agree very well with the WRWS method. The longitudinal permittivity ε_z is not as stable nor as well in agreement with WRWS results as the ε_t results. This is somewhat expected considering the measurement configuration. In an RWG probe, the dominant mode is TE^z_{10}, which does not contain a z-directed electric field component; thus, the tFWMT weakly interrogates ε_z. Even so, the tFWMT configuration produces the improved results over those reported using a similar nondestructive measurement geometry, where, in some cases, ε_z was not reported due to their instability [9].

With regard to the inclusion of higher order modes, Chang *et al.* [9] hypothesized that higher order modes do not significantly affect the results for anisotropic materials. Fig. 6 shows the results when higher order modes are considered. In this case, due to the symmetry of the apertures and for computational efficiency, only $\mathrm{TE}^z_{1(2q)}$ and $\mathrm{TM}^z_{1(2q)}$ (where $q = 0, 1, 2, \ldots, Q$) are considered [5]. From these results, it is apparent that higher order modes do not significantly affect the extracted values for ε_t, but including the TE^z_{12} and TM^z_{12} modes does elicit a significant change on the Im[ε_z] results—bringing the values much closer to the WRWS results. Including the higher order modes does produce a significant change in the Re[ε_z] results, but it is not clear that these results are improved over the dominant-mode-only results. Therefore, it is difficult to draw concrete conclusions from the data at hand about the validity of the hypothesis that dominant-mode-only analysis is sufficiently accurate for most applications. Note that additional modes beyond these two do not contribute significantly to either component.

2) Characterization of Lossy Honeycomb: A uniform insertion loss carbon-loaded honeycomb core was procured from Cuming Microwave. The cells were manufactured with 0.3175 cm (0.125 in.) width and the core was loaded with a proprietary lossy coating rated at 10 dBi/in. Since the material is available in 30.48 cm × 30.48 cm × 1.02 cm (12 in × 12 in × 0.4 in) sheets, a free-space measurement was determined to be the most effective comparison method. The results from the focused beam measurement technique (FBMT) were obtained from measurements made at two different angles of incidence, $\theta_i = 0°$ and $60°$.

Figs. 7 and 8 show the results of the extractions. The agreement between the tFWMT and FBMT results for ε_t is quite excellent. Similar to the low-loss honeycomb material results, the agreement between the tFWMT and reference results in the ε_z case is not as good. This conflict is likely due to the measurement configuration limitation discussed earlier and noted by other researchers [9]. Another source of this disagreement is the inhomogeneity of the sample. Like resistive cards, carbon black was used in the manufacture of the 10-dBi/in lossy honeycomb material. It is very difficult to ensure uniform loading of the carbon black. This issue is well documented [27]–[30]. Additionally, the slopes of the curves for the ε_z parameters indicate that the honeycomb material is slightly dispersive in the z-direction, which would not be unexpected for a uniaxial structure. This behavior is also seen in [31] for similar types of carbon black-based materials. Therefore, since the z-directed electric field interrogates the carbon black walls more strongly than the transverse electric field, the effect is more pronounced in the results for ε_z.

IV. Simulation of Higher Permittivity Materials

In order to more fully characterize the method's utility, the materials described in [32] were simulated in the tFWMT configuration and the results are compared to Knisely's work. The measurement methods utilized in [32] are the single-port waveguide probe (SPWP) method and the usual RWG method for comparison. The SPWP method differs from the tFWMT only in that one waveguide probe is replaced with a perfect electrical conductor (PEC) sheet. Since the SPWP provides a smaller number of measurements, its utility is inherently more limited in fully characterizing complex materials. This article considers two simulated uniaxial materials for comparison—a high contrast material and a single-slab uniaxial material.

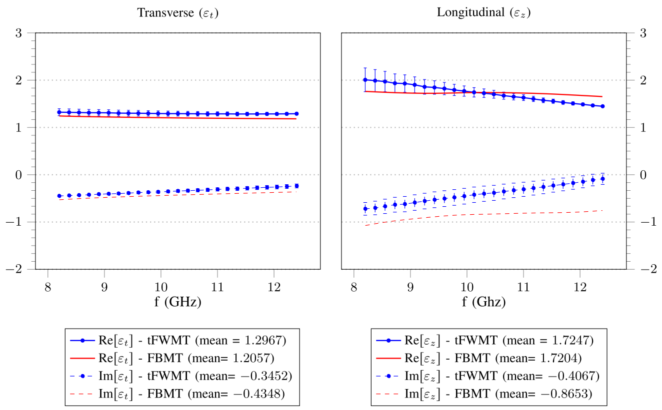

Fig. 7. Results from the tFWMT extraction performed on the lossy 10-dBi/in honeycomb material using only the dominant mode. The error bars are $\pm 2\sigma$.

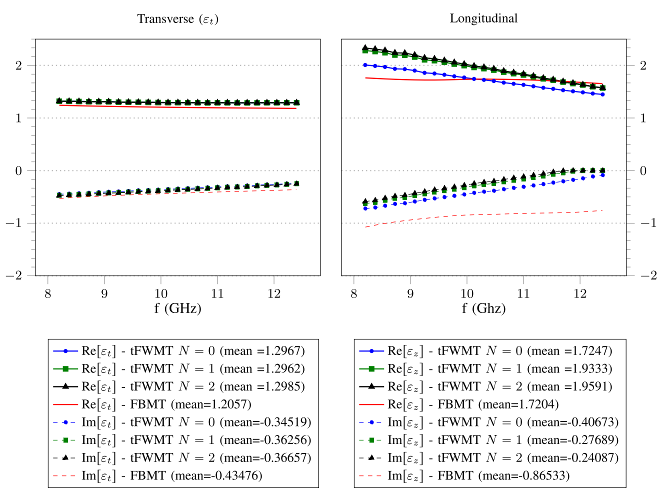

Fig. 8. Results from the tFWMT extraction performed on the lossy 10-dBi/in honeycomb material incorporating higher order modes. Only the $\mathrm{TE}^z_{1(2n)}$ and $\mathrm{TM}^z_{1(2n)}$ modes are considered for $n = 0, 1,$ and 2. Error bars are omitted for visual simplicity.

All simulations were full wave and run using CST Microwave Studio.

A. High Contrast Simulated Material

The high contrast simulated material is composed of a slab material with a specified permittivity of $2.5 - j0.2$ incorporating tetragonal inclusions comprised of a material with a specified permittivity of $9.9 - j0.0$. Each simulation is calibrated by means of a TRL method. The results of the comparison are shown in Fig. 9. The results demonstrate a similar behavior as with the lossy honeycomb material shown in Fig. 6, to include the periodic shape of the longitudinal (ε_z) permittivity curves.

In order to provide one further point of comparison, a single slab of uniaxial material with known dispersive permittivities, ε_t and ε_z, similar to the high contrast material, were simulated in the tFWMT configuration. The results shown in Fig. 10 demonstrate a similar behavior to both previous lab and simulation cases for lossy, high permittivity materials, including a higher uncertainty. This higher uncertainty was determined to

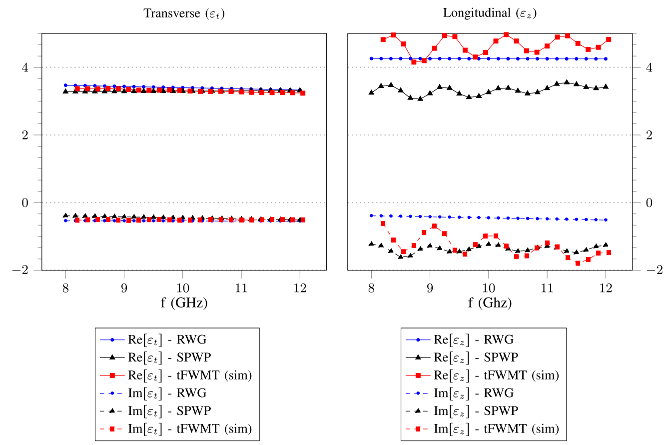

Fig. 9. Comparison of extraction results using the high contrast uniaxial material described in [32]. The RWG probe and SPWP results are directly from the referenced article, while the tFWMT results utilized the same simulated material in a tFWMT simulation, performed in CST. The tFWMT was then employed to extract permittivities from the resulting S-parameters. Only the $\mathrm{TE}^z_{1(2n)}$ and $\mathrm{TM}^z_{1(2n)}$ modes are considered for $n = 0, 1,$ and 2. Error bars are omitted for visual simplicity.

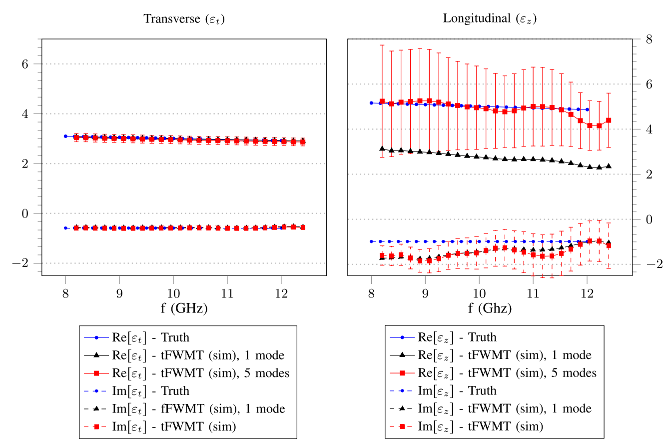

Fig. 10. Comparison of extraction results using the high contrast sample of [32]. In this case, instead of modeling the physical structure of the material, a solid 0.125-in slab of material with known uxiaxial parameters was simulated in the tFWMT geometry, again using CST. Only the $\mathrm{TE}^z_{1(2n)}$ and $\mathrm{TM}^z_{1(2n)}$ modes are considered for $n = 0, 1,$ and 2. In this case, the error bars are displayed to highlight the large uncertainty.

be associated with the S_{12} and S_{21} parameters, which further confirms that this behavior is due to a weak interrogating field in the z-direction.

V. Conclusion

The primary focus of this article was to develop and demonstrate a method for the simultaneous nondestructive extraction of the permittivity and permeability of a uniaxial anisotropic media. The method utilized a single fixture in which the MUT is clamped between two-flanged RWGs. The transmission and reflection coefficients were measured and then compared with the theoretical coefficients to find $\overleftrightarrow{\varepsilon}$ via nonlinear least squares. Both low-loss and lossy uniaxial honeycomb materials were measured using this configuration, and simulations performed to correlate the results to the previously published works. The results for real part of the transverse permittivity were shown to converge to a stable solution utilizing the dominant mode TE^z_{10}, while the imaginary part is shown to converge with the addition of one higher order mode, the TE^z_{12} and TM^z_{12} hybrid mode. As expected, the extracted transverse constitutive parameters were in good agreement with traditional destructive methods. The new technique produced good, but mildly unstable values when extracting the longitudinal parameters, as a result of a weak z-directed electric field component.

With regard to the inclusion of higher order modes, we see acceptable convergence to a stable solution for the extracted longitudinal permittivity values when including two additional modes. This is likely due to the presence of a z-directed electric field in the higher order modes. Regardless of this limitation, this article is a significant contribution to the scientific community because the results are a significant improvement over previous nondestructive methods for anisotropic materials. Therefore, it is recommended to further test this method on a wider range of materials, including both dielectric and magnetic uniaxial materials, in order to assess the precision of the method to simultaneously extract permeability and permittivity.

Furthermore, we note the two physical MUTs considered in this article varied in thickness from 0.25 to 0.4 in. As noted in [5], thicker materials are more accurately measured when including higher order modes in the MFIEs. This was indeed the case, as the measurement of a thinner, low-loss honeycomb showed good agreement while only including the dominant mode. However, the thicker, lossy honeycomb material required inclusion of higher order modes to show better agreement with the reference methods.

Finally, the extraction of ε_t, ε_z, μ_t, and μ_z requires another set of independent measurements, which was not performed due to limited material availability. However, future work could focus on incorporating additional set of independent measurements (such as the TTM) for extraction of a larger number of parameters. Additionally, it is possible that utilizing a slightly different configuration, where the waveguides are placed next to one another and the MUT is backed by a sheet of PEC [7], [27], will allow for improvements in the crack and defect detection of advanced materials when access is limited to a single side of the MUT.

ACKNOWLEDGMENT

The views expressed in this article are those of the authors and do not reflect the official policy or position of the U.S. Air Force, the Department of Defense, or the U.S. Government.

REFERENCES

[1] R. K. Kawakami, E. J. Escorcia-Aparicio, and Z. Q. Qiu, "Symmetry-induced magnetic anisotropy in Fe films grown on stepped Ag (001)," *Phys. Rev. Lett.*, vol. 77, pp. 2570–2573, Sep. 1996. doi: 10.1103/PhysRevLett.77.2570.

[2] D. Gay, *Composite Materials: Design and Applications*. Boca Raton, FL, USA: CRC Press, 2014.

[3] C.-W. Chang, Y. F. Chen, and J. Qian, "Nondestructive determination of electromagnetic parameters of dielectric materials at X-band frequencies using a waveguide probe system," *IEEE Trans. Instrum. Meas.*, vol. 46, no. 5, pp. 1084–1092, Oct. 1997.

[4] G. D. Dester, E. J. Rothwell, and M. J. Havrilla, "Two-iris method for the electromagnetic characterization of conductor-backed absorbing materials using an open-ended waveguide probe," *IEEE Trans. Instrum. Meas.*, vol. 61, no. 4, pp. 1037–1044, Apr. 2012.

[5] M. W. Hyde, IV, and M. J. Havrilla, "A nondestructive technique for determining complex permittivity and permeability of magnetic sheet materials using two flanged rectangular waveguides," *Prog. Electromagn. Res.*, vol. 79, pp. 367–386, 2008.

[6] N. Maode, S. Yong, Y. Jinkui, F. Chenpeng, and X. Deming, "An improved open-ended waveguide measurement technique on parameters ε_r and μ_r of high-loss materials," *IEEE Trans. Instrum. Meas.*, vol. 47, no. 2, pp. 476–481, Apr. 1998.

[7] J. W. Stewart and M. J. Havrilla, "Electromagnetic characterization of a magnetic material using an open-ended waveguide probe and a rigorous full-wave multimode model," *J. Electromagn. Waves Appl.*, vol. 20, pp. 2037–2052, Apr. 2006.

[8] M. D. Seal, M. W. Hyde, and M. J. Havrilla, "Nondestructive complex permittivity and permeability extraction using a two-layer dual-waveguide probe measurement geometry," *Prog. Electromagn. Res.*, vol. 123, pp. 123–142, 2012.

[9] C.-W. Chang and Y. F. Chen, "Nondestructive measurements of complex tensor permittivity of anisotropic materials using a waveguide probe system," *IEEE Trans. Microw. Theory Techn.*, vol. 44, no. 7, pp. 1081–1090, Jul. 1996.

[10] J. Krupka, K. Derzakowski, A. Abramowicz, M. E. Tobar, and R. G. Geyer, "Use of whispering-gallery modes for complex permittivity determinations of ultra-low-loss dielectric materials," *IEEE Trans. Microw. Theory Techn.*, vol. 47, no. 6, pp. 752–759, Jun. 1999.

[11] Y. Xu, "A study of waveguides filled with anisotropic metamaterials," *Microw. Opt. Technol. Lett.*, vol. 41, no. 5, pp. 426–431, 2004.

[12] D. R. Smith, D. C. Vier, T. Koschny, and C. M. Soukoulis, "Electromagnetic parameter retrieval from inhomogeneous metamaterials," *Phys. Rev. E, Covering Stat. Nonlinear Biol. Soft Matter Phys.*, vol. 71, no. 3, 2005, Art. no. 036617.

[13] G. Mumcu, K. Sertel, and J. L. Volakis, "A measurement process to characterize natural and engineered low-loss uniaxial dielectric materials at microwave frequencies," *IEEE Trans. Microw. Theory Techn.*, vol. 56, no. 1, pp. 217–223, Jan. 2008.

[14] Z. Li, K. Aydin, and E. Ozbay, "Determination of the effective constitutive parameters of bianisotropic metamaterials from reflection and transmission coefficients," *Phys. Rev. E, Covering Stat. Nonlinear Biol. Soft Matter Phys.*, vol. 79, no. 2, 2009, Art. no. 026610.

[15] B. Crowgey, J. Tang, O. Tuncer, L. Kempel, E. Rothwell, and B. Shanker, "Measurement of anisotropic material properties for antenna applications," in *Proc. Loughborough Antennas Propag. Conf. (LAPC)*, Nov. 2012, pp. 1–4.

[16] J. Schultz, *Focused Beam Methods: Measuring Microwave Materials in Free Space*. Scotts Valley, CA, USA: Createspace, 2012.

[17] M. Hyde, M. Havrilla, and A. Bogle, "A novel and simple technique for measuring low-loss materials using the two flanged waveguides measurement geometry," *Meas. Sci. Technol.*, vol. 22, no. 8, 2011, Art. no. 085704.

[18] M. W. Hyde IV, M. I. J. Havrilla, and A. E. Bogle, "Nondestructive determination of the permittivity tensor of a uniaxial material using a two-port clamped coaxial probe," *IEEE Trans. Microw. Theory Techn.*, vol. 64, no. 1, pp. 239–246, Jan. 2016.

[19] J. Baker-Jarvis, M. D. Janezic, P. D. Domich, and R. G. Geyer, "Analysis of an open-ended coaxial probe with lift-off for nondestructive testing," *IEEE Trans. Instrum. Meas.*, vol. 43, no. 5, pp. 711–718, Oct. 1994.

[20] R. E. Collin, *Field Theory of Guided Waves*. Piscataway, NJ, USA: IEEE Press, 1991.

[21] N. Rogers, "Nondestructive electromagnetic characterization of uniaxial materials," Ph.D. dissertation, Air Force Inst. Technol., Wright-Patterson Air Force Base, OH, USA, 2014.

[22] N. G. Rogers and M. Havrilla, "Dyadic Green's functions for a parallel plate waveguide filled with anisotropic uniaxial media," *Prog. Electromagn. Res. B*, vol. 63, pp. 249–261, 2015.

[23] G. F. Engen and C. A. Hoer, "Thru-reflect-line: An improved technique for calibrating the dual six-port automatic network analyzer," *IEEE Trans. Microw. Theory Techn.*, vol. MTT-27, no. 12, pp. 987–993, Dec. 1979.

[24] A. Knisely *et al.*, "Biaxial anisotropic material characterization using rectangular to square waveguide," in *Proc. 36th Annu. Symp. Antenna Meas. Techn. Assoc. Conf.*, 2014, pp. 437–442.

[25] A. Knisely and M. Havrilla, "Material characterization de-embedding for rectangular to square waveguide," in *Proc. 9th Eur. Conf. Antennas Propag. (EuCAP)*, Apr. 2015, pp. 1–5.

[26] A. G. Knisely, M. J. Havrilla, and M. W. Hyde, "Material characterization uncertainty analysis for rectangular to square waveguide," in *Proc. USNC-URSI Radio Sci. Meeting (Joint With AP-S Symp.)*, Jul. 2015, p. 98.

[27] M. W. Hyde IV, J. W. Stewart, M. J. Havrilla, W. P. Baker, E. J. Rothwell, and D. P. Nyquist, "Nondestructive electromagnetic material characterization using a dual waveguide probe: A full wave solution," *Radio Sci.*, vol. 44, no. 3, pp. 1–13, Jun. 2009.

[28] B. B. Glover, K. W. Whites, M. W. Hyde, IV, and M. J. Havrilla, "Complex effective permittivity of carbon loaded dielectric films with printed metallic square rings," in *Proc. 2nd Int. Congr. Adv. Electromagn. Mater. Microw. Opt. (Metamaterials)*, 2008, pp. 762–764.

[29] F. Costa, "Surface impedance measurement of resistive coatings at microwave frequencies," *IEEE Trans. Instrum. Meas.*, vol. 62, no. 2, pp. 432–437, Feb. 2013.

[30] J. P. Massman, M. J. Havrilla, K. W. Whites, and M. W. Hyde, "A stepped flange waveguide technique for determining tapered R-card sheet impedance," in *Proc. Asia–Pacific Microw. Conf.*, Dec. 2010, pp. 1769–1772.

[31] M. Hotta, M. Hayashi, M. T. Lanagan, D. K. Agrawal, and K. Nagata, "Complex permittivity of graphite, carbon black and coal powders in the ranges of X-band frequencies (8.2 to 12.4 GHz) and between 1 and 10 GHz," *ISIJ Int.*, vol. 51, no. 11, pp. 1766–1772, 2011.

[32] A. G. Knisely, M. W. Hyde, M. J. Havrilla, and P. J. Collins, "Uniaxial anisotropic material measurement using a single port waveguide probe," in *Proc. AMTA*, Oct./Nov. 2016, pp. 1–6.

Neil Rogers received the B.S. degree in electrical engineering from the University of Tulsa, Tulsa, OK, USA, in 2003, and the M.S. and Ph.D. degrees in electrical engineering from the Air Force Institute of Technology, Wright-Patterson Air Force Base, Dayton, OH, USA, in 2009 and 2014, respectively.

From 2003 to 2007, he was an Acquisitions Officer with the National Air and Space Intelligence Center, Wright-Patterson Air Force Base, Dayton, OH, USA. From 2009 to 2011, he was a Government Researcher with the Air Force Research Laboratory, Kirtland Air Force Base, NM, USA. From 2014 to 2018, he was the Deputy Chief Engineer for the JSTARS Recap Program, Hanscom Air Force Base, MA, USA. He is currently an Associate Professor of electrical engineering with the United States Air Force Academy, CO, USA. His current research interests include electromagnetic material characterization, radar mode development, and electromagnetic scattering and propagation.

Dr. Rogers is also a member of the Eta Kappa Nu and Tau Beta Pi honor societies.

Michael Havrilla (S'85–M'86–SM'05) received the B.S. degrees in physics and mathematics, the M.S.E.E degree, and the Ph.D. degree in electrical engineering from Michigan State University, East Lansing, MI, USA, in 1987, 1989, and 2001, respectively.

From 1990 to 1995, he was with General Electric Aircraft Engines, Evendale, OH, USA, and Lockheed Skunk Works, Palmdale, CA, USA, where he was an Electrical Engineer. He is currently an Associate Professor with the Department of Electrical and Computer Engineering, Air Force Institute of Technology, Wright-Patterson Air Force Base, OH, USA. His current research interests include electromagnetic and guided-wave theory, electromagnetic propagation and radiation in complex media and structures, and electromagnetic materials' characterization.

Dr. Havrilla is also a member of the URSI Commission B and the Eta Kappa Nu and Sigma Xi honor societies.

Milo W. Hyde, IV (S'10–M'10–SM'12) received the B.S. degree in computer engineering from the Georgia Institute of Technology, Atlanta, GA, USA, in 2001, and the M.S. and Ph.D. degrees in electrical engineering from the Air Force Institute of Technology, Wright-Patterson Air Force Base (WPAFB), Dayton, OH, USA, in 2006 and 2010, respectively.

From 2001 to 2004, he was a Maintenance Officer with the F-117A Nighthawk, Holloman Air Force Base, Alamogordo, NM, USA. From 2006 to 2007, he was a Government Researcher with the Air Force Research Laboratory, WPAFB. He is currently an Associate Professor with the Department of Electrical and Computer Engineering, Air Force Institute of Technology. His current research interests include electromagnetic material characterization, guided-wave theory, scattering, and optics.

Dr. Hyde is also a member of the International Society for Optical Engineering, the Optical Society of America, the American Geophysical Union, the Directed Energy Professional Society, and the Applied Computational Electromagnetics Society.

Alexander Knisely received the B.S. degree in electrical engineering from Wright State University, Dayton, OH, USA, in 2012, and the M.S. degree in electrical engineering from the Air Force Institute of Technology (AFIT), Wright-Patterson Air Force Base, Dayton, OH, USA, in 2015, where he is currently pursuing the Ph.D. degree in electrical engineering.

His current research interests include electromagnetic material characterization, guided-wave theory, and electromagnetic propagation and radiation in complex media and structures.